Effect of microstructure on fatigue crack deviation in AA2050-T84

Vladimir A. Esin, Marie François, Lisa Belkacemi, Daniel Irmer, Louise Briez, Henry Proudhon

Highlights

Effect of microstructure on fatigue crack deviation in AA2050-T84

Vladimir A. Esin,Marie François,Lisa T. Belkacemi,Daniel Irmer,Louise Briez,Henry Proudhon

- Fatigue crack deviation in AA2050-T84 mostly occurs at GBs;
- GBs in T84 state are weakened by PFZ and/or solute GB segregation;
- Grains in AA2050-T84 have "layered" strained structure favourable for crack deviation inside the grains.

Effect of microstructure on fatigue crack deviation in AA2050-T84

Vladimir A. Esin[a,*], Marie François[a], Lisa T. Belkacemi[b,c], Daniel Irmer[a], Louise Briez[d] and Henry Proudhon[a]

[a]Centre des Matériaux (UMR CNRS 7633), Mines Paris, PSL University, Évry, France
[b] Leibniz-Institute for Materials Engineering-IWT, Bremen, Germany
[c]Department of Microstructure Physics and Alloy Design, Max-Planck Institut für Eisenforschung, Düsseldorf, Germany
[d]Dassault Aviation, Saint-Cloud, France

ARTICLE INFO

Keywords:
AA2050
crack deviation
grain boundary
intermetallics
precipitate free zones

ABSTRACT

Precipitation hardened AA2050 exhibits an unusual crack deviation phenomenon during fatigue testing: when the intended crack propagation direction is not parallel to macroscopic rolling direction, after initial propagation perpendicular to the loading direction, the crack deviates and further abnormally propagates in other direction which can be parallel to the direction of applied loading. Such a behaviour renders difficult the prediction of cracking in AA2050 and, thus, of AA2050 fatigue lifetime. In the present work using multi-scale microstructure characterization (SEM/EBSD/EDX, transmission electron microscopy (TEM) and atom probe tomography (APT)) of AA2050-T84 after fatigue tests, the effect of different microstructure parameters on crack deviation is carefully investigated keeping constant the macroscopic mechanical conditions (sample geometry, loading direction and amplitude, frequency). The respective influence of grain structure (including that of grain boundaries), intermetallics and precipitate-free zones is evaluated. The grain boundaries with misorientation angle ranging from 40 to 60° are observed to be the origin of the deviation phenomenon: the principal crack deviates at grain boundaries and further propagates along grain boundary. Numerous Fe- and Mn-rich intermetallics found in the volume of AA2050-T84 do not represent the major cause for the crack deviation, although, fostering it (only 25% of cracks were observed to deviate in the regions containing the intermetallics). The cause of failure at grain boundaries was deduced from APT results and TEM observation of precipitate free zones comparing T84 and T34 states (the latter do not reveal the crack deviation). In addition, it was observed that because of unrecrystallized state of AA2050-T84, the grains feature "layered" strained structure favourable to deviation inside the grains when a critical internal misorientation is reached along the crack path.

1. Introduction

One of the biggest challenges faced by aerospace engineers is designing innovative aluminium alloys which are lighter and possess better mechanical properties than existing alloys. The use of Al-Li system for aerostructures provides great advantages due to their reduced density compared to conventionally employed aluminium alloys. These emerging alloys have enhanced mechanical properties such as increased stiffness and fracture toughness, higher fatigue crack growth resistance and corrosion resistance [1]. The widespread interest for Al-Li alloys is driven by potential for weight reduction by lithium addition: 1% wt. of Li leads to 3% of alloy weight reduction and in parallel increases the Young modulus by 6% [2]. However, Al-Li alloys exhibit an unusual failure mode which still limits their use in aerospace industry [3–6].

Different parts of aeronautic structures are subjected to repetitive loadings due to, for example, successive take-offs and landings. It can lead to rupture by fatigue. The first stages of fatigue crack initiation and micro-propagation are still not well understood although they represent an important part of the service lifetime of the parts. In Al-Li alloys, during crack propagation under fatigue conditions in the direction which is not parallel to the rolling direction and perpendicular to the applied force (mode I), the crack deviates and might propagate along the direction of the applied force [7, 8]. Such a phenomenon in AA2050-T8 was naturally and almost exclusively studied using a mechanical approach. Nevertheless, the multiscale character of aluminium alloys microstructure might have a direct effect on the origin of crack deviation. However, very few data on microstructure influence on crack deviation in aluminium alloys are available in the literature.

First, the impact of hardening phases on fatigue crack deviation phenomenon relies on the nature of precipitates, being either shearable or not shearable by dislocations. It is admitted that shearable precipitates do not disturb planar dislocation glide and, hence, should not impact the crack propagation direction [9]. On the contrary, in the case of non-shearable precipitates, cross slip can occur which might lead to further crack deviation [10, 11]. AA2050-T8 is mostly hardened by T_1-Al_2CuLi [12] phase which can be both sheared and bypassed [13–17]. The presence of hardening phases is usually accompanied by the formation of precipitate free zones (PFZ) close to high angle grain boundaries due to solute consumption in the adjacent bulk areas required for precipitate formation at grain boundaries [18, 19]. The width of the PFZ, whose formation is diffusion controlled, depends on temperature, time and alloy composition [20].

*Corresponding author
vladimir.esin@minesparis.psl.eu (Vladimir A. Esin); jessicafrancois12@outlook.com (M. François); lissa.belkacemi@gmail.com (L.T. Belkacemi); daniel.irmer@minesparis.psl.eu (D. Irmer); louise.briez@dassault-aviation.com (L. Briez); henry.proudhon@minesparis.psl.eu (H. Proudhon)
ORCID(s):

Table 1
Chemical composition (wt. % and at. %) of AA2050 used for the present study.

Elements	Cu	Li	Mg	Ag	Zr	Zn	Si	Fe	Ti	Al
wt. %	3.2-3.9	0.7-1.3	0.2-0.6	0.2-0.7	0.06-0.14	<0.25	<0.08	<0.1	<0.1	bal.
at. %	1.4-1.7	2.7-5.0	0.2-0.7	0.05-0.17	0.02-0.04	<0.1	<0.07	<0.05	<0.06	bal.

Such PFZ were shown to decrease the performances of AA6165-T6 (Al-Si-Mg-Cu) during tensile tests [21]. Moreover, the toughness was decreased as well in the presence of PFZ due to crack propagation along grain boundaries. It can thus be expected that PFZ have an effect on fatigue crack deviation. Second, even for the alloy with shearable precipitates, fatigue crack deviation can be observed due to different grain crystal orientation (no crystal texture). In Al-Li alloys, cracks usually follow {111} dislocation slip planes and, in the case of non textured materials, the crack will naturally change the propagation direction at grain boundaries moving from grain to grain [9, 10, 22]. Finally, Al alloys can contain several (often harmful) intermetallic inclusions due to presence of impurities, like Fe. They are formed during processing and are not eliminated during the final heat treatment. These inclusions can reach the size of several microns and often be grouped and aligned with the rolling direction [23]. They can be the site for fatigue crack initiation leading to rupture [24]. However, the effect of the intermetallic inclusions on crack deviation is not investigated in detail.

Therefore, the aim of the present work was to evaluate the respective role of different microstructure features on crack deviation in AA2050-T84 under the same fatigue crack propagation conditions (same charge, amplitude and charged direction) and for a given microstructure (the mechanical behaviour is not reported).

2. Material and Methods

The studied AA2050 was produced by Constellium and supplied as 100 mm-thick sheets in overaged T84 state. The chemical composition is given in Table 1 in wt. % as well as in at. % for the sake of simplicity. The Young's modulus, yield and ultimate tensile strength at room temperature were 77 GPa, 495 and 522 MPa, respectively.

Fatigue tests were carried out in lab air using compact tension (CT) samples with a thickness of 10 mm, machined at the quarter thickness of the initial sheet. The maximum force of 6 kN with R=0.1 was applied along the rolling direction (RD) and the crack was intended to grow along the normal direction (ND) to the RD-TD rolling plane (TD is the transverse direction)) (Figure 1). A particular attention has been paid to the location of CT-samples machining to have exactly the same residual stresses for every used sample, as it can affect crack propagation phenomenon [25].

After fatigue tests performed until sample failure, multi-scale microstructure characterization was carried out. Grain structure was analyzed using scanning electron microscopy

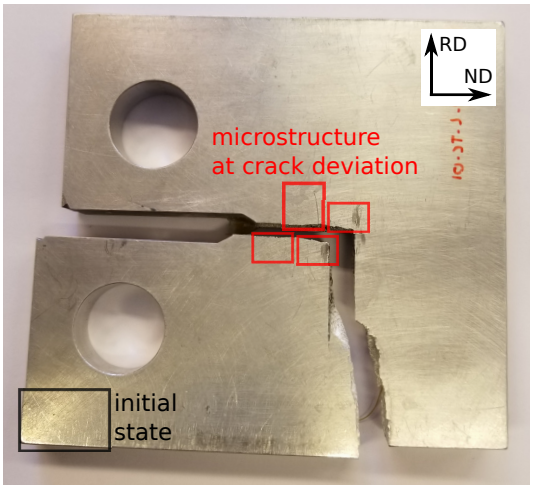

Figure 1: CT sample after fatigue test which led to crack deviation. Different areas used to machine samples for microstructure analysis are indicated.

(SEM) S-FEG FEI Nova NanoSEM 450 and electron backscatter diffraction (EBSD) using an acceleration voltage of 20 kV. The intermetallic inclusions were observed using the backscatter electrons (BSE) mode and their composition was evaluated by electron dispersive spectroscopy (EDS). The samples were prepared by standard metallographic procedure which consisted in machining in different CT sample areas (Figure 1), nickel electrodeposition to protect the fractured surface, embedding in resin, grinding and polishing. For EBSD analyses, the samples were additionally polished during 24 h using vibrating polisher and colloidal silica. The obtained EBSD maps were analyzed with OIM 7.0 software taking 5° as a cut-off value to distinguish two adjacent grains [26, 27]. As the grains are large (as will be shown later), their size was measured using index quality (IQ) maps superposed with grain boundary (GB) maps from EBSD and applying the intercept method. The "strain" state was analyzed using both grain orientation spread (GOS) and Kernel Average Misorientation (KAM) criteria [26, 28]. Grains with a GOS value less than 2° were considered as not strained, since only conventional (not high resolved) EBSD analyses were carried out [29]. The microstructure observation at the nanoscale level was performed using FEI Tecnai F20-ST transmission electron microscope (TEM) operating at 200 kV. To prepare TEM thin foils, cylinders of 3 mm in diameter were first obtained by electron discharge machining (EDM) (Figure 1). Second, 300 µm-thick discs were cut and further mechanically thinned down to about

100 µm. The final step consisted in electrochemical jet polishing in a mixture of nitric acid and methanol (1:3) at -30 °C using a voltage of 9 V.

To investigate the chemical composition of grain boundaries, atom probe tomography (APT) was chosen as it gives access to the 3D solute distribution with a nearly atomic scale resolution. APT relies on the field evaporation of atoms located on the surface of a needle-shaped specimen exhibiting a radius of curvature less than 100 nm. A site-specific lift-out procedure was applied to prepare APT specimens using a ThermoFisher, Dual Beam Helios G4 Cxe plasma focused ion beam scanning electron microscope (PFIB/SEM, Leibniz-Institut für Werkstofforientierte Technologien - IWT, Bremen, Germany). The wedge was extracted from a region containing a grain boundary, mounted onto standard Si micro-post coupons from Cameca Instruments and cut into individual mounts. The latter were sharpened using a low acceleration voltage of 8 kV and a decreasing current ranging from 1 nA to 10 pA. The last cleaning step was applied at 5 kV and 10 pA in order to remove the contaminated top layer of the thin needle-shaped specimen. During the PFIB-milling and sharpening, transmission Kikuchi diffraction (TKD) measurements were performed iteratively in order to trace the grain boundary within the specimen and adjust the annular milling patterns in such a way that the grain boundary is preserved from being milled by the focused Xe-plasma ion beam. The needle-shaped specimens were analyzed by a LEAP 5000XR APT (Leibniz-Institut für Werkstofforientierte Technologien - IWT, Bremen, Germany), using the voltage pulsing mode, at 50 K, a detection rate of 0.5 % (0.005 detected ions per pulse), with a high voltage pulse amplitude of 15% of the DC voltage applied to the specimen and a pulse repetition rate of 125 kHz. The obtained volumes were reconstructed and processed using the commercial Cameca's APSuite (6.1) software, using standard algorithms as described in [30–32]. The measured composition of Al-Li and Al-Mg based alloys by APT is known to be affected by the temperature and the pulse fraction due to preferential evaporation [33], especially when the laser-pulsing mode is used. In this work, only the high-voltage mode was employed to ensure the reliability of the results, and great care was taken in the choice of the analysis parameters described above, in line with [33].

3. Results

To get insight into the effect of microstructure on crack deviation in AA2050-T84, first, a multiscale characterization of the as-received T84 state was carried out.

3.1. AA2050-T84 in as-received state

The CT samples for crack propagation tests were machined from the 100 mm-thick sheets of AA2050-T84 after all processing steps, including rolling. First, to characterize the microstructure corresponding to the as-received state, the grain structure, as well as the intermetallic inclusions, were investigated along different planes in relation to RD, far from the crack growth region (see Figure 1 for the location of machined samples).

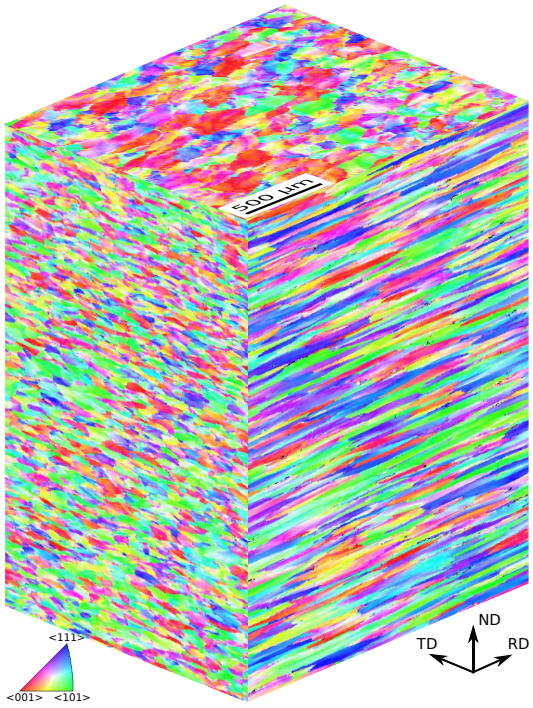

Figure 2: Pseudo-3D grain orientation map obtained by EBSD for AA2050-T84 in as-received state. Each colour gives the orientation in the normal direction of respective plane.

3.1.1. Grain structure

The grain structure was essentially characterized using EBSD which gives access to grain size and morphology, crystal texture as well as the residual deformation state inside the grains in the form of lattice curvature [28]. A pseudo-3D orientation map of grains in AA2050-T84 is shown in Figure 2, where each color gives the orientation in the normal direction of the respective plane. One can clearly see that the grain morphology and the orientation are different in different planes. The grain size was carefully measured along the three main planes using the intercept method and the maximum, minimum, mean values together with the standard deviation (std) were obtained along different directions. To characterize the grain size anisotropy, the aspect ratios (ratio of the mean grain size along the two principal perpendicular directions for a given plane) were calculated. The results are reported in Table 2. One can see that the mean grain size varies from about 30 to about 300 µm and the grains are extremely elongated along RD in the RD-ND plane, with an aspect ratio of 10. It is worth reminding that ND was chosen as the initial crack propagation direction, with the load applied in the direction parallel to RD.

A more detailed EBSD analysis of the microstructure in the RD-ND plane is given in Figure 3, where the orientation map together with GB, GOS and KAM maps are shown. The variation of crystal orientation for a given grain can be observed in the orientation map (Figure 3a). It suggests the

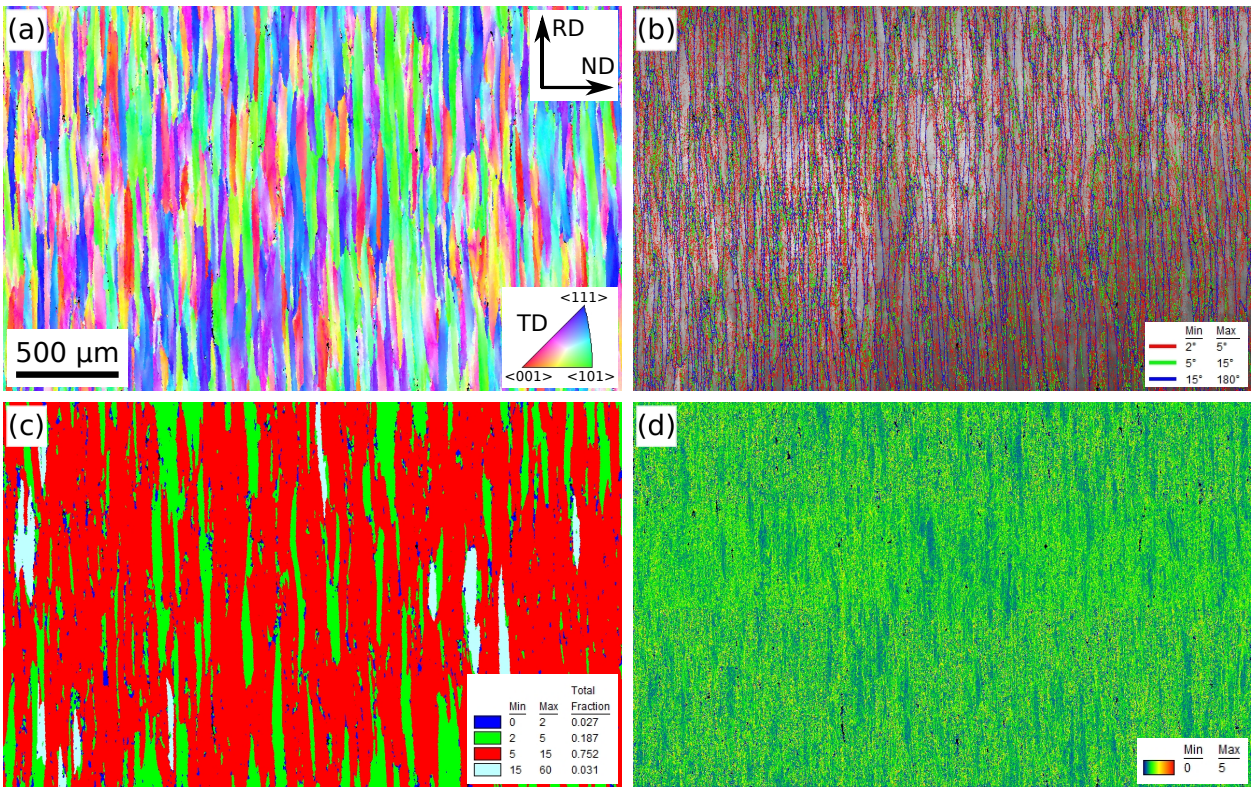

Figure 3: Microstructure analysis of AA2050-T84 using EBSD in RD-ND plane: (a) orientation map according to normal direction to RD-ND plane, (b) GB map superposed with index quality (IQ), (c) GOS map and (d) KAM map.

Table 2
Grain size (µm) in AA2050-T84 in different planes relative to rolling direction (RD).

Plane	TD-RD		TD-ND		RD-ND	
Direction	TD	RD	TD	ND	RD	ND
Mean	67	213	106	26	289	28
Maximum	74	250	144	32	373	31
Minimum	56	167	89	23	207	25
Std	8	24	20	3	56	2
Aspect ratio	3		4		10	

presence of some residual strain in AA2050-T84 in the as-received state (after all the processing steps). The GB map reveals a number of sub-grain boundaries, mostly situated close to high-angle GBs (Figure 3b). A more detailed analysis using GOS and KAM maps (Figure 3c and d), reveals a very strained state of grains with 70% of grains having interior misorientation between 5 and 15° which is more or less homogeneously distributed. Only a very low portion of grains and regions appear as not strained, with a GOS value less than 2°) and a KAM value close to 0 respectively. These results clearly indicate the non-recrystallized state of AA2050-T84.

3.1.2. Intermetallic inclusions

As many aluminium-based alloys, AA2050 contains inclusions of intermetallic phases inherited from the alloy processing, which cannot be dissolved during the solutioning treatment. An exhaustive study of their morphology, size and spatial distribution was carried out by Nizery et al. using 3D X-ray tomography [23]. According to these results, AA2050 contains only Al-Cu–Fe–Mn intermetallic compounds, with the largest size along RD that can reach several tens of microns.

A micrograph showing typical inclusions of intermetallic phases in the studied AA2050-T84 is shown in Figure 4. According to EDS analyses, they can be divided into two groups: Fe-rich and Mn-rich. The former seems to correspond to the $Al_7Cu_2(Fe,Mn)$ phase often found in aluminium based alloys [34, 35] and to be significantly larger than Mn-rich intermetallics. Fe-rich intermetallic particles were observed as packets and were cracked during the processing along the direction perpendicular to RD [23] while Mn-rich intermetallic particles were mostly aligned along RD.

3.1.3. Hardening precipitates and PFZ

AA2050 was subjected to an ageing treatment to induce precipitation hardening and thereby obtain the T84 state. After ageing, the alloy should mostly contain T_1-Al_2CuLi second phase precipitates, which are known to be both sheared and bypassed by dislocations. These precipitates are formed as platelets in {111} planes of the aluminium matrix. Despite their small size (which was evaluated to be of 150 nm in diameter), these precipitates could be first observed using SEM (Figure 5a). One can see both well

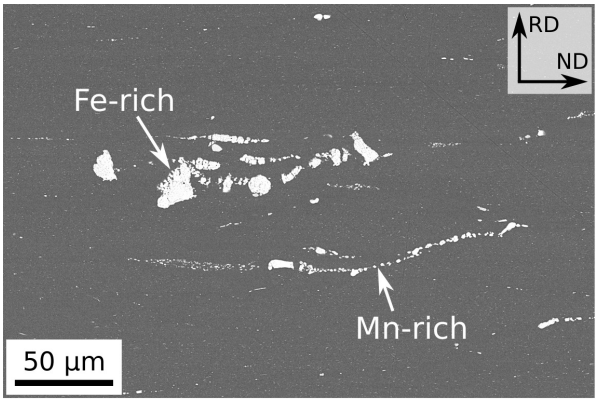

Figure 4: Inclusions of intermetallic phases in AA2050-T84 as observed by SEM/BSE in RD-ND plane.

organized bulk precipitates, together with continuous chains of GB precipitates. The advantage of SEM observations lies in the high number of grains and GBs that could be analyzed. More detailed analyses using TEM revealed that even several sub-grain boundaries constitute precipitation sites for the T_1 phase, which can clearly follow sub-grain boundary steps (Figure 5b). The correlation between the precipitation at sub-grain boundaries and their properties, e.g. misorientation angle and thus energy, could not be clearly established. It is worth noting that, due to increased grain size in the studied AA2050 (Table 2), only very few GBs were contained in each TEM sample. Nevertheless, PFZ were systematically observed close to GBs. These PFZs, as compared to other aluminium based alloys, could be observed on one side of the GB and exhibited an uncommonly low width of 40 nm (Figure 5c), without shedding any doubt on their presence. However, a recent work by Mansouri Arani et al. showed that strain localization is observed even for such narrow PFZ [36].

3.2. Microstructure at crack deviation

To carry out post-mortem studies of the effect of microstructure on crack deviation, a specific experimental procedure was established for the microstructure characterization in the region where the crack deviation takes place.

3.2.1. Fractographic observations

First, the fracture surface was observed at low magnification (Figure 6). The surface is rather smooth close to the notch and becomes wavier towards the crack deviation. To get insight into the crack propagation and deviation phenomena, SEM observations using SE and BSE regimes (to reveal the presence of intermetallic compounds) were done in different regions of the fracture surface. Close to the notch, the surface is almost flat, with some classic fatigue strips and very few intermetallic inclusions (Figure 7a). When approaching the crack deviation, in agreement with Figure 6, the surface becomes wavy and more intermetallic particles can be observed. Moreover, micro-cracks can be clearly seen whose number, length and opening seem to increase when moving closer to the crack deviation (Figure 7b and c). Such micro-cracks were observed as well during fatigue load of AA2090 (Al-Cu-Li family) [3]. For the present AA2050-T84, these cracks can be associated with the intermetallic inclusions, as shown in Figure 7b, but also be situated or developed in the regions without intermetallic particles. Such an increase in the number of intermetallic inclusions onto the fracture surface when moving from the notch to the crack deviation, as well as the micro-cracks associated to these inclusions, might suggest an important role of intermetallic inclusions in the crack propagation mechanism and, therefore, crack deviation in AA2050-T84.

From the fracture surface observation, one can conclude that the principal crack deviation, leading to sample rupture, is preceded by a number of micro-cracks formed along the direction perpendicular to that of the initial crack propagation, and then propagated along the same direction as the principal crack deviation. It is thus reasonable to assume that the reasons for the crack deviation "location" (i.e. the distance from the notch) is mainly defined by mechanics while the microstructure features responsible for crack deviation should be the same for micro-cracks and for the principal crack. Accordingly, a deep microstructure analysis was performed in the regions close to micro-cracks in order to look for the common microstructure parameters. Such postmortem analyses are not straightforward in the region of the main deviation, since a number of artifacts can be induced during the sample preparation of fracture surfaces of the initial CT sample. Interrupted crack propagation tests could not be carried out in the present work. Therefore, the effect of microstructure on crack deviation in AA2050-T84 was further mainly studied using 2D observations performed using the samples prepared, according to the scheme shown in Figure 8. To get more insight into the 3D character of the studied phenomenon, a high number of 2D observations was done to increase statistics.

3.2.2. Effect of intermetallics

As it was shown before, Fe- and Mn-rich intermetallic inclusions were observed in AA2050-T84: they are aligned along RD over several hundreds of microns (Figure 4). To study the role of intermetallic inclusions in crack deviation, a number of observations was carried out in the RD-ND plane on samples prepared according to Figure 8. Since the studied phenomena is in 3D, at least 30 micro-cracks in 2D micrographs were observed, to be able to draw reliable conclusions. The zone of the initial crack propagation is situated at the bottom part of the micrographs presented in Figure 9. The thick bright layer in the bottom part corresponds to the nickel coating deposited to protect the crack propagation surface during sample preparation, as explained in Material and Methods section. As the intermetallic inclusions and the nickel layer have a very close contrast in SEM/BSE regime, EDS measurements were systematically carried out to distinguish between the intermetallic inclusions and the nickel layer, thereby avoiding misinterpretation of experimental results. Such observations using SEM revealed that in about

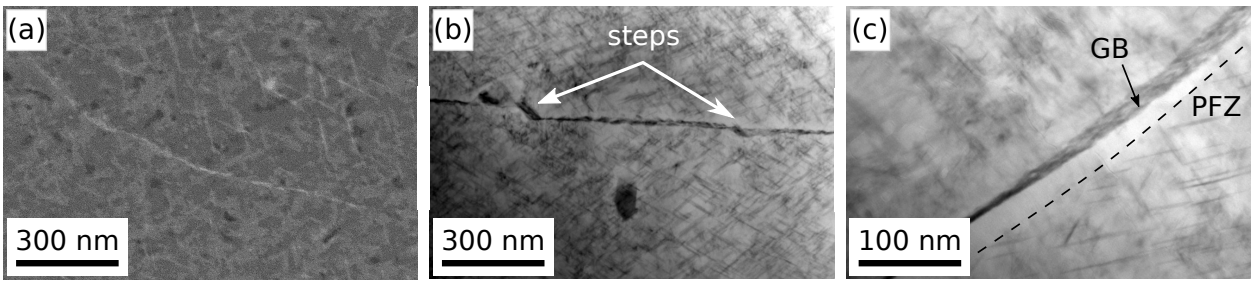

Figure 5: Observation of hardening precipitation of T_1-Al_2CuLi phase in AA2050-T84: a) precipitates in grains and at GB observed using SEM, b) sub-grain boundary precipitates observed using TEM (zone axis close to <101>) and c) GB precipitates and PFZ observed using TEM.

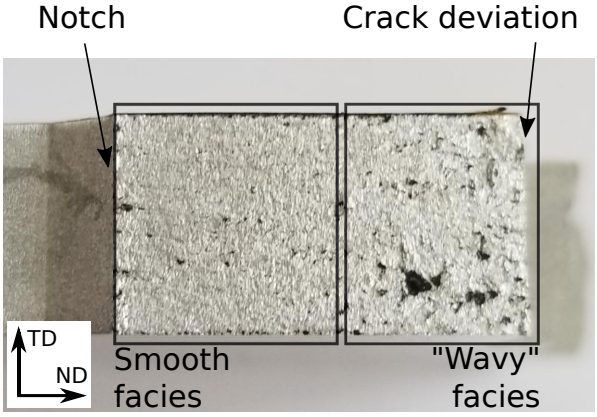

Figure 6: Fracture surface after fatigue crack propagation test which led to crack deviation.

75% of cases, the micro-cracks were formed far from intermetallic inclusions (Figure 9a). Moreover, the alignments of these intermetallic inclusions could be completely "ignored" by micro-cracks in several cases (Figure 9b). For 25% of observed micro-cracks, they were formed along the intermetallic inclusions aligned with RD, as shown in Figure9c. Therefore, one can conclude that the intermetallic inclusions are not the main initiation site of the crack deviation in AA2050, although they can contribute to the phenomenon.

3.2.3. Effect of grain structure

According to the microstructure analysis of AA2050-T84 in the as-received state, the grain structure is very anisotropic, the largest grain size of about 400 µm was observed along RD and the grains were remarkably elongated in the RD-ND plane, as compared to other planes (Table 2). Such a grain structure anisotropy is expected to have an effect on the crack growth during the fatigue test and further crack deviation. Grain structure in the RD-ND plane of interest in the CT sample areas containing micro-cracks was accurately investigated using EBSD after the crack propagation test has been finished, and the sample fractured. The same sample preparation methodology, as described in Figure 8 for investigation of intermetallic inclusions, was applied for 2D observations using EBSD. Once again, due to the 3D character of the studied phenomena, a number of EBSD acquisitions was carried out at both CT sample surface and at mid-thickness, allowing for general conclusions.

First, *all* the micro-cracks were observed to propagate along GBs for depths in the vicinity of the initial crack propagation path (which corresponds to the first moments of micro-cracks formation) at both mid-thickness and CT sample surface (Figure 10). Therefore, GBs seem to be the preferential micro-crack initiation site and might be the origin of the final crack deviation. One can observe as well that, after propagation along GBs, the micro-cracks can deviate, propagate perpendicularly to the initial GB until reaching the neighboring GB and deviate again, forming a step-like propagation path at both mid-thickness and CT sample surface. It is thus concluded that the same microstructure features govern crack propagation and deviation at mid-thickness and CT sample surface. The discussion can henceforth be limited to the phenomena observed at the CT sample surface.

A more detailed analysis of micro-cracks gives insight into microstructure parameters which can lead to their deviation and, therefore, the deviation of the main initial crack. One can see that the micro-crack on the right-hand side in Figure 10b initiates at a GB, then propagates along RD, changes its propagation direction and, finally, reaches again the same GB. The micro-crack on the left-hand side in Figure 10b has a more complex step-like propagation path with two "steps". Further EBSD analyses, performed with an acquisition step of 200 nm (much finer than 1.5 µm used to obtain Figure 10) were carried out in the regions where the two steps (or deviations) were observed. The orientation maps together with the GB misorientation angle maps are shown in Figure 11.

One can notice that the "upper" deviation is preceded by micro-crack propagation along GBs parallel to RD, then the micro-crack propagation changes and follows the trajectory almost parallel to ND and then, perpendicular to the initial propagation path (Figure 11a). A sawtooth morphology of crack propagation path can be seen, which seems much more pronounced for the lower part of the micro-crack fracture surface. Finally, the micro-crack reaches the neighboring GB, deviates and propagates along GB parallel to RD. Over the course of the micro-crack propagation along a GB parallel to RD, a second "step" is observed (Figure 11b). The crack deviates in a direction between ND and RD showing

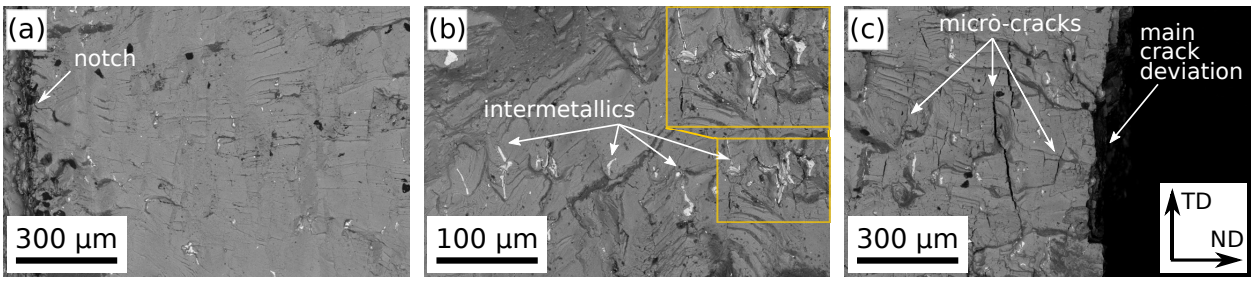

Figure 7: Fracture surface observation using SEM/BSE in different regions: a) close to the notch, b) close to crack deviation and c) at crack deviation.

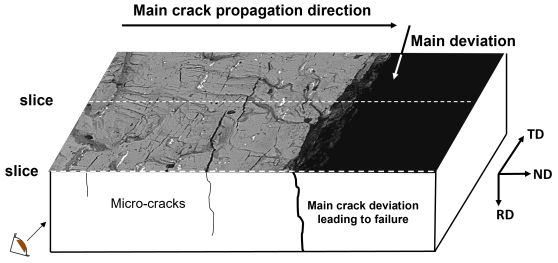

Figure 8: Scheme for sample preparation for 2D microstructure characterization in the areas close to micro-cracks.

a sawtooth morphology (once again much more pronounced for a lower fracture surface) before deviating again and continuing along RD; the last deviation does clearly not occur at GB. Moreover, the micro-crack deviation is not affected by the presence of intermetallic inclusions, indicated by black arrow in Figure 11b, suggesting their secondary effect on crack deviation in AA2050-T84. It is thus concluded that despite the initial GB propagation along RD, the micro-crack can deviate several times.

Figures 11c and d represent GB misorientation angle superimposed with IQ maps for the same areas shown in Figures 11a and b, respectively. The "upper" micro-crack deviation occurs in the grain with a lot of sub-grain boundaries due to the non recrystallized state of AA2050-T84 (Figures 11c). However, the "lower" deviation is observed in a grain with no sub-structure (Figures 11d). Therefore, sub-grains and sub-grain boundaries, formed during the processing and further heat treatment, do not seem to be the origin of crack deviation phenomena in AA2050-T84. It should be mentioned however that such a conclusion might be mitigated by 3D effects.

4. Discussion

The fatigue crack growth tests of AA2050-T84 carried out in the present work in RD-ND configuration (where RD is parallel to the load direction and ND is parallel to initial crack propagation direction) led to crack deviation *always* observed along RD. The results obtained in this work reveal the critical role of GBs in crack deviation. The initial crack meets a GB every 25 µm along ND, whereas much less often along RD (every 289 µm) (see Table 2). It is worth noting that the crack propagation tests carried out with AA2050-T84 where the initial crack propagation was parallel to RD (which corresponds to elongation direction of grains (Figure 2)) did not lead to crack deviation [7, 8] which agrees with the conclusion on the importance of GBs on crack deviation phenomena in AA2050-T84. The intermetallic inclusions seem to contribute to the crack deviation but they are not essential to induce the phenomenon, since only $\frac{1}{4}$ of observed micro-cracks paths were associated to the inclusions of intermetallic compounds (Figure 9). However, even though a micro-crack can grow along GBs parallel to RD, it can further deviate several times forming a "step-like" propagation path (Figure 11a and b). The reasons for such a deviation have to be carefully examined since they can reveal the mechanisms on micro-scale level of the initial crack deviation leading to the CT sample rupture.

4.1. GB misorientation angle

First, the GB misorientation angle was analyzed in the region of occurrence of micro-cracks with help of the OIM 7.0 software. The two micro-cracks observed in Figure 10a initiate at GBs with a misorientation angle of 47 (on the left-hand side) and 52° (on the right-hand side), respectively. For the micro-crack observed on the right-hand side in Figure 10b, this angle is of 38°; the micro-crack observed on the left-hand side initiates at one GB and almost immediately deviates to propagate along another GB. The misorientation angles for these GBs are 59 and 52°, respectively. Therefore, it seems that micro-cracks (and the deviation of the main initial crack) take place at general high-angle GBs with misorientation angle ranging from 40 to 60°.

4.2. Mean grain and local misorientation

The as-received T84 state of AA2050 indicates that the alloy was strained during the processing: first, after the homogenization treatment and quenching and, second, after ageing to peak hardness. Such a quite complex processing route resulted in a non-recrystallized state of AA2050-T84 where the grains were observed to have more or less pronounced internal misorientation (Figure 3). The effect of such grains on micro-crack initiation was investigated using GOS maps for regions in Figure 10 where the micro-cracks were observed. The grains with a GOS value less than 2° were considered as not having internal misorientation [26,

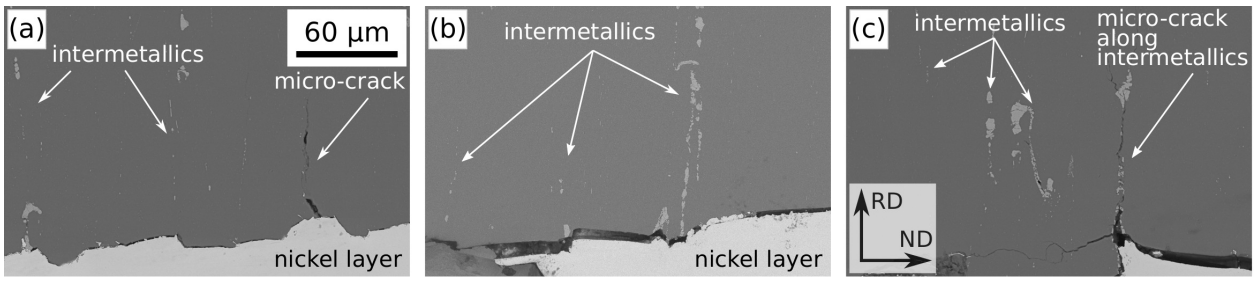

Figure 9: Effect of intermetallic inclusions on micro-crack formation during crack propagation test of AA2050-T84: a) micro-crack formed far from intermetallics (for 75% of the micro-cracks observed), b) no micro-cracks formed despite intermetallics alignments and c) micro-cracks formed along intermetallics alignment (for 25% of the micro-cracks observed). A thick bright layer in the bottom part of micrographs corresponds to nickel coating used to protect initial crack propagation surface. The micrographs were obtained with the same magnification and in the same RD-ND plane.

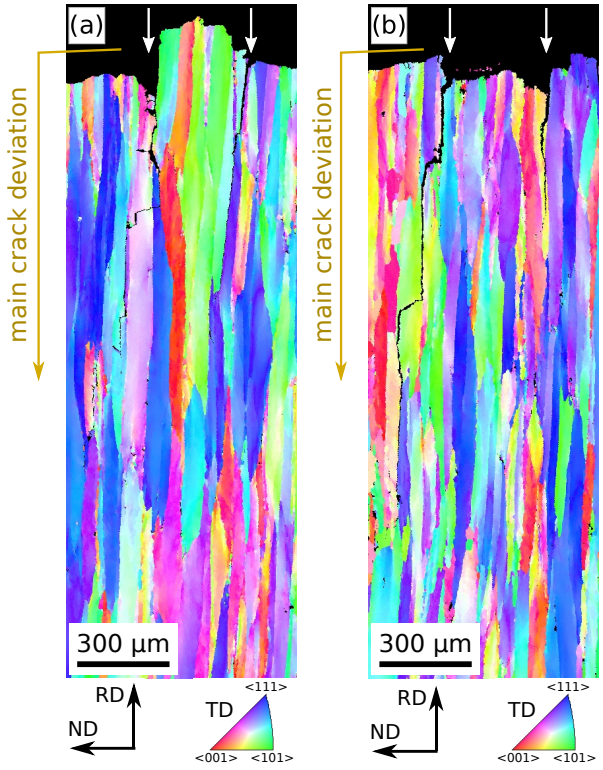

Figure 10: Orientation maps in TD for the same CT sample after crack propagation test: a) at mid-thickness and b) close to sample surface. The micro-cracks initiation sites are indicated by white arrows, the main crack propagation and deviation direction are also shown (the upper ("black") parts of the figures correspond to the fracture surface of the samples).

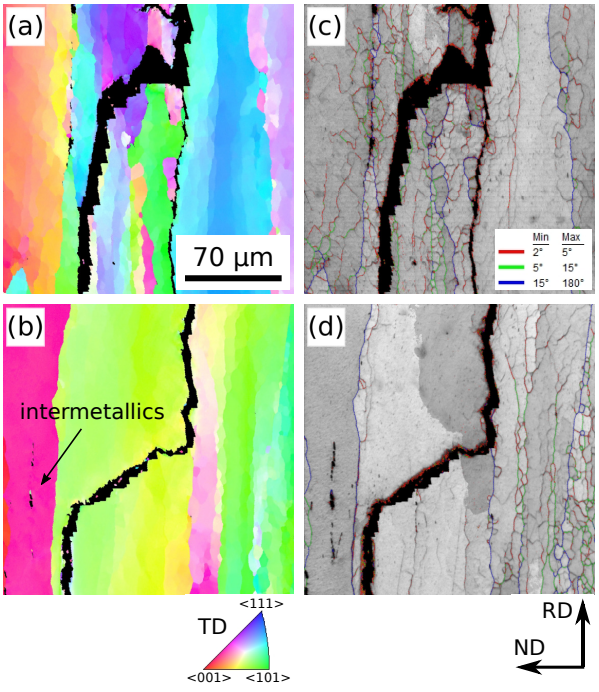

Figure 11: EBSD analysis with acquisition step of 200 nm in the two regions of micro-crack deviation observed in Figure 10b. Orientation maps in TD for a) "upper" deviation and b) "below" deviation and c) and d) corresponding GB misorientation angle superposed with IQ maps.

29]. GOS maps shown in Figure 12a and c for the micro-cracks presented in Figure 10 indicate that the micro-cracks can initiate and propagate between the grains exhibiting similar GOS values: between 2 and 5° in Figure 12c. The micro-crack on the right-hand side in Figure 12a initiates between the grains with different GOS values. For the micro-crack on the left-hand side in Figure 12a, the initiation takes place between "highly strained" grains (with increased similar GOS values from 5 to 15°), then the micro-crack propagates between grains with different GOS values and finally between the grains with the same low GOS value from 2 to 5°. Therefore, no clear correlation between micro-crack initiation at GBs and internal misorientation of the adjacent grains can be observed.

The strain-induced local misorientation can be investigated using KAM maps which are often related to the so called geometrically necessary dislocations (GND) [27, 37–41]. While GOS criterion is a grain property, KAM gives information in a localized area inside the grain [28]. KAM maps considering the first neighbor and a cut-off value of 5° were obtained for the areas for which orientation and GOS maps were already discussed (Figure 12b and d). The micro-cracks turn out to initiate in both high KAM value

(thus, of higher dislocation density) and low KAM value regions. Therefore, no correlation with local misorientation and micro-crack initiation at GBs and propagation can be unambiguously established.

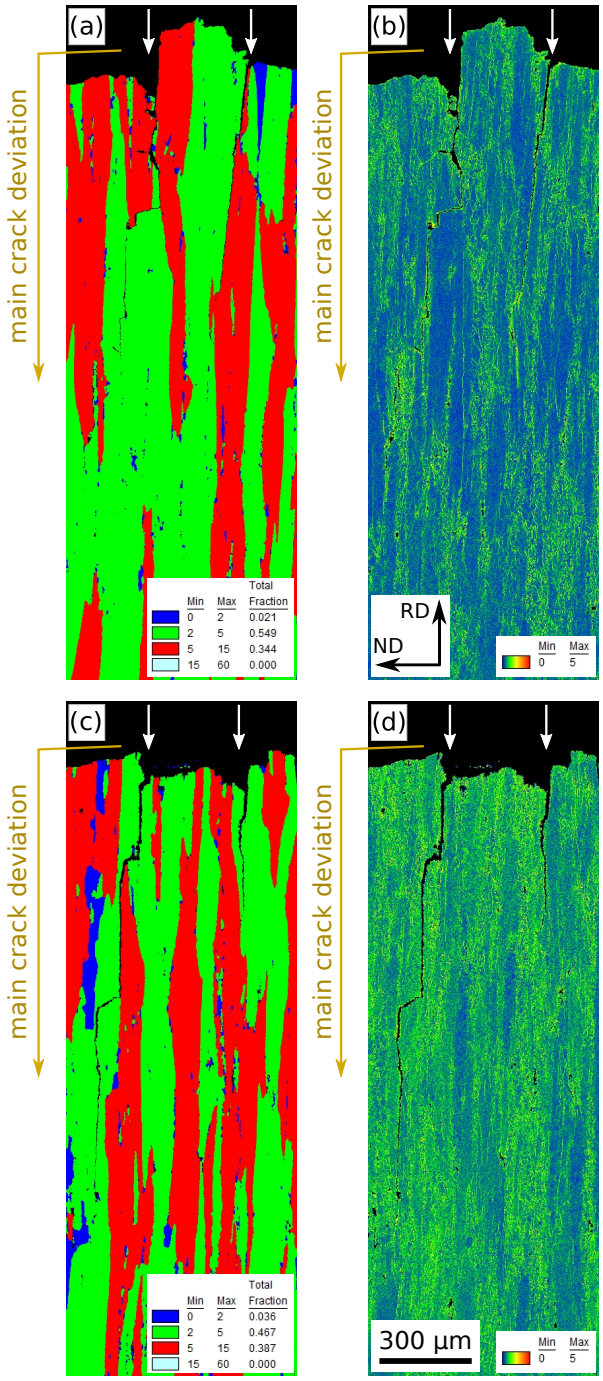

Figure 12: Strain analysis using EBSD in the areas where the micro-cracks were observed to initiate and propagate: a) GOS and b) KAM maps for the area analysed in Figure 10a and c) GOS and d) KAM maps for the area analysed in Figure 10d. The micro-cracks initiation sites are indicated by white arrows, the main crack propagation and deviation direction are also shown.

4.3. Intragranular misorientation

The orientation map obtained with an acquisition step of 200 nm shown in Figure 11b reveals a continuous variation of crystal orientation inside the same grain, associated to the non-recrystallized state of AA2050-T84. To understand the physical reasons for the micro-crack deviation (and thus for the main initial crack), the evolution of intragranular orientation was investigated along the crack propagation path. For this, the orientation maps for the same analysis area were determined along the direction parallel to RD (which corresponds to micro-crack propagation along GB, Figure 13a) and along the direction parallel to ND (which corresponds to micro-crack propagation after deviation, Figure 13c); the orientation map in Figure 11b is plotted according to TD. Several orientation profiles were plotted as well for both orientation maps (Figure 13b and d). These orientation profiles give the misorientation of the given pixel as compared to the first pixel in the profile.

When analyzing the orientation evolution along RD (Figure 13a and b), one can see that it continuously increases from the first analyzed pixel towards the area where the micro-crack deviation takes place (profiles 1-3 in Figure 13b). These observations suggest that the crack deviation occurs when a critical misorientation in the same grain is progressively reached. According to the results obtained along RD, it can be estimated to be close to 5°. The orientation map of the same area, plotted along ND, clearly reveals layered-like crystal structure of the grain: an increase in the misorientation is continuously observed from one GB to another along ND, but the grain is composed of layers of almost constant crystal orientations (Figure 13c and d). As for the crack propagation along RD, it seems that a critical misorientation value exists, leading to crack deviation. For ND, according to the profile 3 in Figure 13d, it is close to 8°. It is worth noting that the crystal misorientation along ND (propagation direction of the initial crack) can reach 15° (!) inside the same grain (profile 4 in Figure 13d) which is quite a high value. Such intragranular evolution of crystal orientation has a direct impact on the mechanical response: the crack, when propagating along ND, experiences a different mechanical behaviour of the grain due to the evolution, for example, of slip plane orientation. The critical effect of the intragranular misorientation along ND is emphasized by the second micro-crack deviation in Figure 13c observed before the micro-crack reached the GB. Interestingly, the sawtooth-like character of micro-crack propagation seems to correlate with the crystal structure of the grain. It is worth noting that the edges of the "sawteeth" correspond to traces of the {111} aluminium crystal planes, which are the dislocation slip planes in fcc metals.

4.4. Grain boundary brittleness

It seems that GBs represent weakened areas for the crack propagation in AA2050-T84 since the crack systematically deviates at GB (like it was observed for AA2297 [1] and other Al-Li alloys [3]). To get insight into the crack deviation

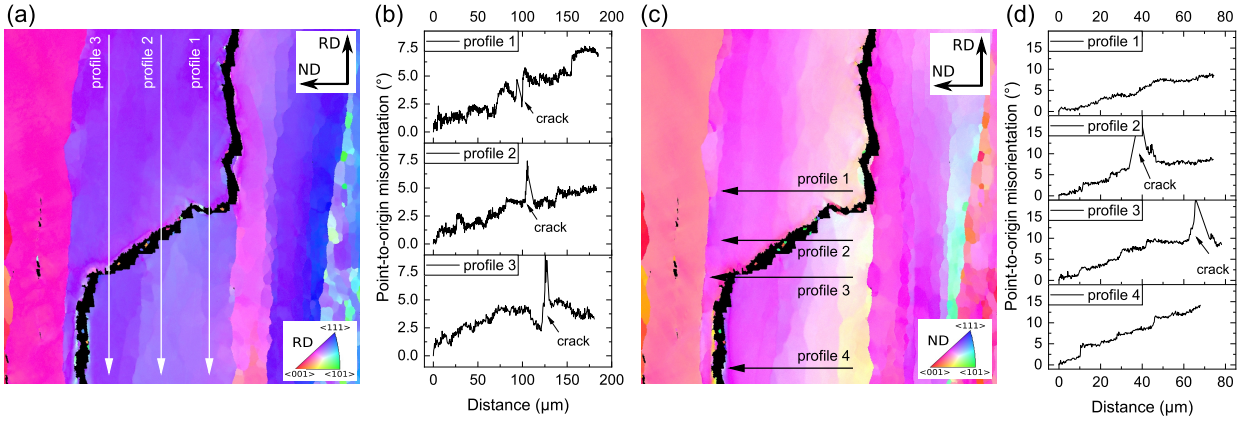

Figure 13: Orientations maps for the region of micro-crack propagation analysed in Figure 10a plotted a) in RD, b) in ND with corresponding c) and d) orientation profiles which give the misorientation of the given pixel as compared to the first pixel in the profile.

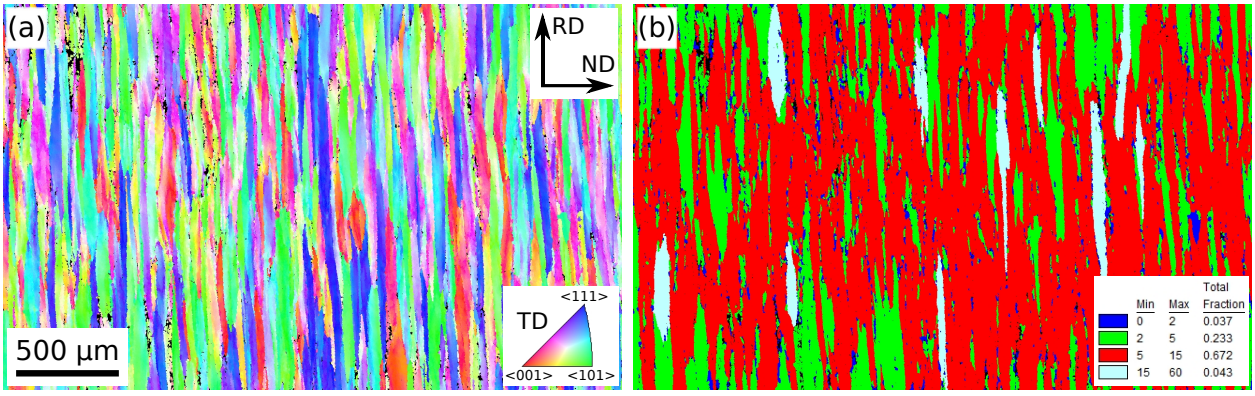

Figure 14: Grain structure analysis in AA2050-T34 using EBSD: a) orientation map in TD and b) corresponding GOS map.

phenomenon, the AA2050-T34, exhibiting a different microstructure, was produced and tested under the same fatigue crack growth conditions as previously applied for the T84 state. Indeed, this paper focuses on the lone effect of the microstructure on crack propagation and its mechanics is beyond the scope of the current work. Fatigue tests of the AA2050-T34 sample did not reveal crack deviation, contrary to the AA2050-T84 sample. First, T34 and T84 states differ in terms of yield stress, as the former did not undergo ageing, directly related to the microstructure. As discussed previously, AA2050-T84 exhibits hardening precipitates corresponding to the T_1 phase, GBs with precipitates and thin PFZ close to GBs (Figure 5). In the same way, the microstructure of AA2050-T34 was characterized using EBSD and TEM.

EBSD analyses revealed no significant difference of the grain structure in terms of morphology and size (Figure 14a and Table 3). Moreover, T34 and T84 states have a very similar strain state, according to GOS criteria (Figure 14b).

Therefore, the difference in crack propagation behaviour between the T34 and T84 states of AA2050 should be explained by other parameters. TEM investigations using selected area electron diffraction (SAED) show that no T_1 second phase precipitate is present in the T34 state (Figure 15). GB crosses the view field and can be observed due to darker contrast as compared to adjacent grains. Quasi-spherical particles observed in Figure 15 were identified as dispersoids (formed during the processing and present in T84 state as well) with a particular role to limit grain growth during the processing and further heat treatment. GBs are free of precipitates and therefore no PFZ is observed either (Figure 15). The existence of the PFZ was suggested to lead to crack formation and propagation in GB containing areas of AA6165 [21]. Therefore, this mechanism can be excluded in the case of the T34 state.

Table 3
Grain size (μm) in AA2050-T34 in different planes relative to rolling direction (RD).

Plane	TD-RD		TD-ND		RD-ND	
Direction	TD	RD	TD	ND	RD	ND
Mean	85	253	106	28	301	35
Std	18	45	9	1	62	2
Aspect ratio	3		4		9	

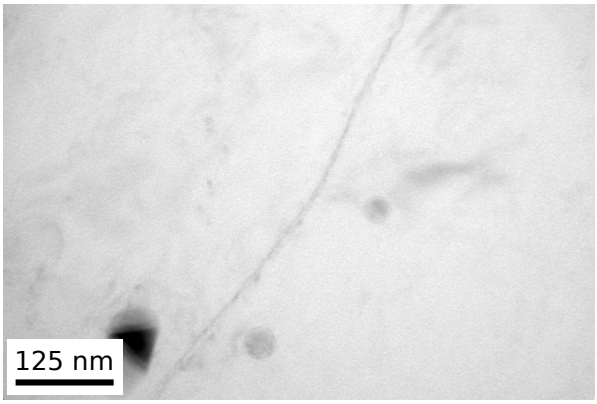

Figure 15: Observation of AA2050-T34 microstructure using bright field analysis in TEM in GB containing area.

On the other hand, GB brittleness can be also dependent on their own composition, as a number of segregating solutes are known to induce alloys embrittlement. Increased solute segregation in AA2050-T84 can be indeed expected as compared to AA2050-T34, since the ageing treatment carried out to obtain peak hardness might be favorable to GB segregation. To measure the local enrichment in solutes within and in the vicinity of GBs in the T34 and T84 samples, APT was employed, as it gives unique insights into the composition of microstructural defects, when the latter are chemically different.

As described in the Material and Methods section, TKD measurements were performed iteratively with the sharpening steps of APT samples in order to guarantee the presence of the targeted GBs within the final needle-shaped specimens. Figure 16 shows the obtained inverse pole figure (IPF) maps overlaid with the image quality (IQ) maps for both the T34 (Figure 16a) and the T84 (Figure 16b) states. The TKD maps reported here were obtained at an intermediate step of the FIB sharpening, as the number of the transmitted electrons onto the diffraction camera screen, i.e. the signal, decreases as the specimen gets thinner.

Figure 17a shows the distribution of Cu, Li, Mg and Ag in the 3D reconstructed volume of the T34 state. These 3D maps illustrate Cu, Mg and Ag enrichment at the GB positioned edge on. A closer analysis has been carried out on the GB and its surrounding to understand the distribution of Li. The signature of the GB going through the specimen (indicated with the red arrows in Figure 17b) can be clearly seen on the detector multiple hit map presented (top), obtained for the whole analyzed volume and in agreement with the IPF map presented in Figure 16a. The single hit map (Figure 17b, bottom), where the crystallographic directions (poles) are readily identifiable, shows the presence of a pole next to the GB, as encircled in white and black. This pole is associated with the Cu-rich line going along the needle-shaped specimen and the depletion in Li along this same direction (Figure 17c and d). Solute enrichment or depletion at crystallographic poles observed by APT is a

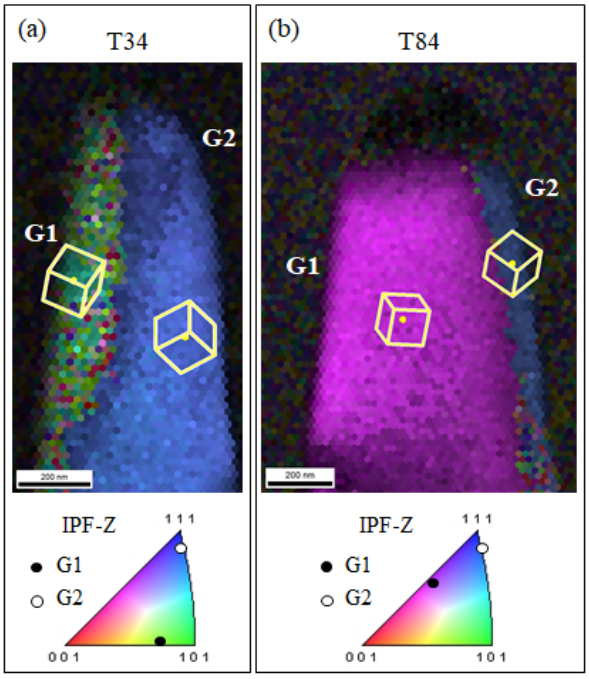

Figure 16: Inverse pole figure (IPF) crystal direction maps overlaid with image quality (IQ) maps, displaying the high-angle grain boundaries obtained by FIB/TKD in (a) the T34 state and (b) the T84 state.

well-known phenomenon resulting from the ion trajectories aberrations inherent to crystalline materials subjected to field evaporation [42–44], and corresponding to the deviation of atoms on the edge of the terraces forming a pole [45]. Correspondingly, the slight decrease in Li content observed on the left side of the GB (Figure 17a and on the one-dimensional composition profile in Figure 17e) is only due to the aberrations inherent to the physics of the field evaporation process and should not be interpreted as reflecting the actual Li distribution in the material of interest. Figure 17e demonstrates that the Li content is different from one grain to another, going from approximately 2.5 at. % on the left side of the GB to approximately 1 at. % on the right side of the GB. As the current work focuses on solute segregation on GBs, Li distribution at the mesoscopic scale is beyond the scope of the present paper. Interestingly, Figure 17e and corresponding values reported in Table 4 also reveal that, already at the T34 state, the GB is slightly enriched in Li, Cu and Mg with contents reaching 3.3 ± 0.093, 2.3 ± 0.073 and 1.4 ± 0.061 at. % respectively.

The same protocole has been applied to the APT analysis of the T84 state sample, in order to determine the chemical composition of the GBs after overageing (in the GB areas free from the precipitates of T_1 phase). The results are shown in Figure 18, where the distribution of Cu, Li, Mg and Ag (as depicted in Figure 18a) show a strong enrichment in Cu, Mg and Ag. Here again, the behaviour of Li requires more investigation to be understood.

First, the iso-concentration surfaces within the GB are reported in Figure 18b, from an edge-on view on the left

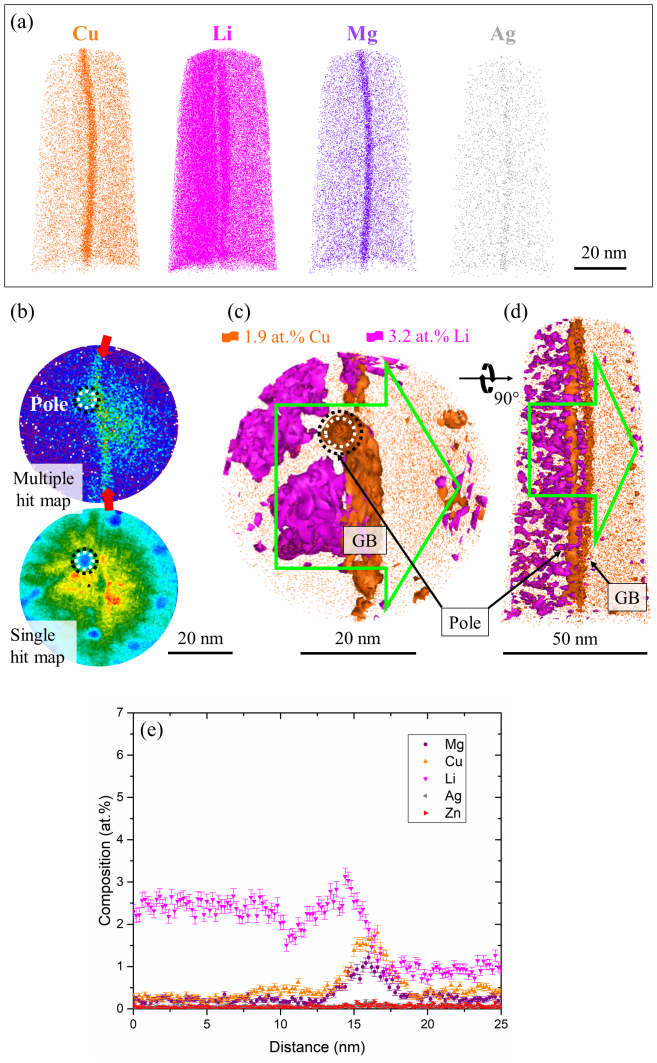

Figure 17: Results of APT analysis of GB composition in AA2050 in T34 state: (a) 3D distribution maps of Cu, Li, Mg and Ag atoms; (b) detector multiple (top) and single (bottom) hit maps obtained over the whole volume of analysis. Distribution of Cu atoms overlaid with the iso-concentration surfaces of Cu and Li, viewed (c) from the top and (d) rotated by 90° to show the grain boundary edge-on and the region of interest used to calculate the one-dimensional composition profile in (e).

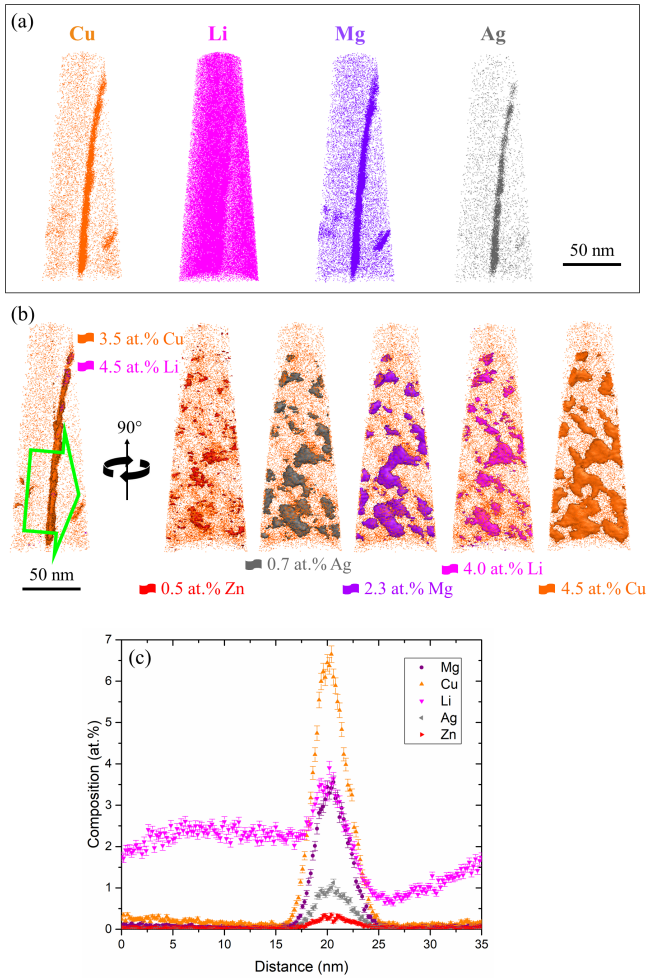

Figure 18: Results of APT analysis of GB composition (in the areas free from precipitates of T_1 phase) in AA2050 in T84 state: (a) 3D distribution maps of Cu, Li, Mg and Ag atoms; (b) distribution of Cu atoms overlaid with the iso-concentration surfaces of Cu and Li, viewed with the grain boundary positioned edge-on (left) and from the perspective of the GB normal (in-plane view) (right) to show the Zn, Ag, Mg, Li and Cu rich isolated islands spread across the grain boundary. The light green arrow indicated on the left corresponds to the region of interest used to calculate the one-dimensional composition profile in (c).

side and from the perspective of the GB normal (in-plane view) for the Zn, Ag, Mg, Li and Cu. The calculation of these iso-concentration surfaces reveals that these elements form solute-rich islands that are spread across the GB plane. Figure 18c presents the one-dimensional composition profile computed perpendicularly to the GB plane, as indicated with the green arrow in Figure 18b. The concentration evolution across the GB accounts for both the solute-rich isolated islands and the less rich regions of the GB, and thereby gives the average solute content within the GB. The core composition of the small solute-rich islands is given in Table 4. The Cu concentration reaches 9.7 ± 0.087 at. %, i.e. 6 times of that in the bulk of the grain. Li and Mg segregation is also significant, exhibiting a core concentration of 5.3 ± 0.063 and 6.6 ± 0.070 at. %, respectively. Besides, a significant segregation of Ag and Zn occurred. Their content in solute-rich isolated islands within the GB (2.1 ± 0.039 and 0.52 ± 0.019 at. % respectively) reaches 90 and 15 times, respectively, their content in the bulk (0.023 and 0.034 at. % respectively). The chemical composition of these islands is significantly different from that of T_1 phase and they were clearly formed due to solute GB segregation induced by overageing (since no solute-rich islands were observed at GB in T34 state). Such islands (or clusters) and solute redistribution at GB have been recently observed in different metallic alloys and different theoretical treatments of the phenomenon were proposed [46–54]. The nature, the

Table 4
Chemical composition (at. %) of GBs in AA2050 in the T34 and T84 states. The values given for the T84 state correspond to the core concentration of solute-rich islands present within the GB.

State	Cu	Li	Mg	Ag	Zn
T34	2.3 ± 0.077	3.3 ± 0.093	1.4 ± 0.061	0.11 ± 0.017	0.11 ± 0.017
T84	9.7 ± 0.087	5.3 ± 0.063	6.6 ± 0.070	2.1 ± 0.039	0.52 ± 0.019

properties and the effect of these GB islands on properties of AA2050 should be further investigated.

Generally, the segregation of an element to GB is accompanied by the depletion of this same element near the GB, before reaching the bulk concentration value as moving away from the GB. In the present case, the depletion is observed on one side of the GB only (Figure 18c). This observation is in good agreement with the TEM observations reporting the presence of a PFZ on one side of the GB only as well (Figure 5c). The relation between the asymmetry of Li composition profile and the existence of a one-sided PFZ needs to be studied further.

We can conclude thus that despite similar grain structure as compared to T34 state, AA2050 in T84 state possess GBs enriched by alloying elements as well as precipitates of T_1 phase leading to the formation of PFZ. All these microstructure features should have a significant effect on resistance of GBs to crack propagation.

Finally, it is worth mentioning that the comparison of the T34 and T84 states and their response to crack propagation behaviour under fatigue conditions cannot be only based on their microstructure, since they possess different mechanical properties that might influence the crack propagation path. Besides the naturally increased yield strength and mechanical resistance of the T84 state, as compared to those of T34 state, different plasticity homogeneity can be expected. Deschamps et al. showed for AA2198 and AA219 that the presence of T_1 second phase precipitates in the peak aged or overaged state leads to much more homogeneous and reverse plasticity when compared to T351 state (without T_1 precipitates) [17]. Moreover, the presence of T_1 precipitates decreases the strain hardening rate. Such a result was explained by specific interactions between dislocations and precipitates. The dislocation activity at a crack tip is a well known phenomenon in ductile materials [55, 56]. Therefore, modification of dislocation motion might affect, as well, crack growth and deviation.

5. Conclusions

The fatigue crack deviation in AA2050-T84 was investigated and the main conclusions of the present work can be summarized as follows:

- the crack deviation is observed when the fatigue test is carried out in the RD-ND configuration (where the load direction is parallel to RD and the initial crack propagation direction is parallel to ND);
- numerous micro-cracks form along ND on the principal crack propagation path and are the precursors of the main crack deviation;
- the crack deviation is of GB character and occurs at high-angle GBs with misorientation angles ranging from 40 to 60°;
- the intermetallic inclusions are not responsible for the crack deviation phenomenon but can facilitate crack growth (only 25% of cracks were observed to form in the regions containing the intermetallics);
- the crack deviation can occur inside the grains when a critical crystal misorientation angle (between 5 and 10°) is reached along the crack propagation path due to the non-recrystallized state of AA2050-T84;
- GBs seem to be weakened by PFZ and/or solute GB segregation in AA2050-T84, as compared to AA2050-T34, where no crack deviation was observed.

CRediT authorship contribution statement

Vladimir A. Esin: Conceptualization, Formal analysis, Investigation, Writing - Original Draft, Writing - Review & Editing, Visualization, Supervision, Project administration, Funding acquisition. **Marie François:** Formal analysis, Investigation, Validation, Writing - Original Draft, Writing - Review & Editing, Visualization. **Lisa T. Belkacemi:** Formal analysis, Investigation, Validation, Writing - Original Draft, Writing - Review & Editing, Visualization. **Daniel Irmer:** Formal analysis, Investigation, Writing - Review & Editing. **Louise Briez:** Conceptualization, Writing - Review & Editing, Supervision, Project administration, Funding acquisition. **Henry Proudhon:** Conceptualization, Writing - Review & Editing, Supervision, Project administration, Funding acquisition.

Data Availability

The raw/processed data required to reproduce the above findings cannot be shared at this time due to legal/ ethical reasons.

References

[1] M.R. Joyce, M.J. Starink, and I. Sinclair. Assessment of mixed mode loading on macroscopic fatigue crack paths in thick section Al–Cu–Li alloy plate. *Materials & Design*, 93:379–387, 2016.

[2] Enrique J. Lavernia and Nicholas J. Grant. Aluminium-lithium alloys. *Journal of Materials Science*, 22(5):1521–1529, May 1987.

[3] M. C. Messner, A. J. Beaudoin, and R. H. Dodds. Mesoscopic modeling of crack arrestor delamination in Al–Li: primary crack shielding and $${T}$$-stress effect. *International Journal of Fracture*, 188(2):229–249, Aug 2014.

[4] P.S. De, R.S. Mishra, and J.A. Baumann. Characterization of high cycle fatigue behavior of a new generation aluminum lithium alloy. *Acta Mat.*, 59(15):5946–5960, 2011.

[5] I. Sinclair and P.J. Gregson. Mixed mode fatigue crack growth in the commercial Al-Li alloy, 8090. *Scripta Metallurgica et Materialia*, 30(10):1287–1292, 1994.

[6] K. T. Venkateswararao, W. Yu, and R. O. Ritchie. Fatigue crack propagation in aluminum- lithium alloy 2090: Part I. long crack behavior. *Metallurgical Transactions A*, 19(3):549–561, Mar 1988.

[7] Sjoerd O. Van Der Veen, Hugo P. Dijkers, and Rene C. Alderliesten. *Anisotropic Fatigue Crack Growth in High-Strength Aluminium Alloys*, pages 1–11. 2016.

[8] Abderrahman Guelzim, Alain Köster, Vincent Maurel, Vincent Chiaruttini, and Érembert Nizery. Crack deviation in thick rolled plates of 2050-T8 Aluminum Alloy. In *The 7th International Conference on Crack paths*, 2021.

[9] M Lewandowska, J Mizera, and J.W Wyrzykowski. Cyclic behaviour of model al–li alloys: effect of the precipitate state. *Materials Characterization*, 45(3):195–202, 2000.

[10] K.T. Venkateswara Rao, R.J. Bucci, K.V. Jata, and R.O. Ritchie. A comparison of fatigue-crack propagation behavior in sheet and plate aluminum-lithium alloys. *Materials Science and Engineering: A*, 141(1):39–48, 1991.

[11] A.K Vasudevan, K Sadananda, and K Rajan. Role of microstructures on the growth of long fatigue cracks. *International Journal of Fatigue*, 19(93):151–159, 1997.

[12] Ph Lequeu, K. P. Smith, and A. Daniélou. Aluminum-copper-lithium alloy 2050 developed for medium to thick plate. *Journal of Materials Engineering and Performance*, 19(6):841–847, 2010. Cited By :128.

[13] J.C Huang and A.J Ardell. Addition rules and the contribution of δ' precipitates to strengthening of aged Al-Li-Cu alloys. *Acta Metallurgica*, 36(11):2995–3006, 1988.

[14] J. M. Howe, J. Lee, and A. K. Vasudévan. Structure and deformation behavior of T1 precipitate plates in an Al- 2Li- 1 Cu alloy. *Metallurgical Transactions A*, 19(12):2911–2920, Dec 1988.

[15] J.F Nie and B.C Muddle. On the form of the age-hardening response in high strength aluminium alloys. *Materials Science and Engineering: A*, 319-321:448–451, 2001.

[16] Aladar A. Csontos and Edgar A. Starke. The effect of inhomogeneous plastic deformation on the ductility and fracture behavior of age hardenable aluminum alloys. *International Journal of Plasticity*, 21(6):1097–1118, 2005. Plasticity of Multiphase Materials.

[17] A. Deschamps, B. Decreus, F. De Geuser, T. Dorin, and M. Weyland. The influence of precipitation on plastic deformation of Al–Cu–Li alloys. *Acta Materialia*, 61(11):4010–4021, 2013.

[18] B. Cai, B.L. Adams, and T.W. Nelson. Relation between precipitate-free zone width and grain boundary type in 7075-T7 Al alloy. *Acta Materialia*, 55(5):1543–1553, 2007.

[19] E. J. Lavernia, T. S. Srivatsan, and F. A. Mohamed. Strength, deformation, fracture behaviour and ductility of aluminium-lithium alloys. *Journal of Materials Science*, 25(2):1137–1158, 1990.

[20] S.C. Jha, T.H. Sanders, and M.A. Dayananda. Grain boundary precipitate free zones in Al-Li alloys. *Acta Metallurgica*, 35(2):473–482, 1987.

[21] T.F. Morgeneyer, M.J. Starink, S.C. Wang, and I. Sinclair. Quench sensitivity of toughness in an Al alloy: Direct observation and analysis of failure initiation at the precipitate-free zone. *Acta Materialia*, 56(12):2872–2884, 2008.

[22] Haigen Jian, Jian Luo, Xianmin Tang, Xue Li, and Cheng Yan. Influence of microstructure on fatigue crack propagation behaviors of an aluminum alloy: Role of sheet thickness. *Engineering Fracture Mechanics*, 180:105–114, 2017.

[23] E. Nizery, H. Proudhon, J.-Y. Buffiere, P. Cloetens, T.F. Morgeneyer, and S. Forest. Three-dimensional characterization of fatigue-relevant intermetallic particles in high-strength aluminium alloys using synchrotron X-ray nanotomography. *Philosophical Magazine*, 95(25):2731–2746, 2015.

[24] H. Weiland, J. Nardiello, S. Zaefferer, S. Cheong, J. Papazian, and Dierk Raabe. Microstructural aspects of crack nucleation during cyclic loading of AA7075-T651. *Engineering Fracture Mechanics*, 76(5):709–714, 2009. Material Damage Prognosis and Life-Cycle Engineering.

[25] Raphaël Cusset, Farida Azzouz, Jacques Besson, Henry Proudhon, Marta Dragon-Louiset, and Vincent Jacques. Effect of residual stress and strain on the fatigue crack propagation in Al2024-T351 structures. *ICF 2017 - 14th International Conference on Fracture*, 1:225 – 226, 2017.

[26] Hiba Fekiri, Vladimir A. Esin, Vincent Maurel, Alain Köster, and Yves Bienvenu. Microstructure evolution of innovative thermal bridge composite (i-TBC) for power electronics during elaboration. *Materials & Design*, 137:68–78, 2018.

[27] O. Muránsky, L. Balogh, M. Tran, C.J. Hamelin, J.-S. Park, and M.R. Daymond. On the measurement of dislocations and dislocation substructures using EBSD and HRSD techniques. *Acta Materialia*, 175:297–313, 2019.

[28] Stuart I. Wright, Matthew M. Nowell, and David P. Field. A review of strain analysis using electron backscatter diffraction. *Microscopy and Microanalysis*, 17(3):316–329, 2011.

[29] A. Nicolaÿ, J.M. Franchet, J. Cormier, H. Mansour, M. De Graef, A. Seret, and N. Bozzolo. Discrimination of dynamically and post-dynamically recrystallized grains based on EBSD data: application to Inconel 718. *Journal of Microscopy*, 273(2):135–147, 2019.

[30] Geiser B. P. Larson D. J. Oltman E. Gerstl S. Reinhard D. Kelly T. F. and Prosa T. J. Wide-field-of-view atom probe reconstruction. *Microscopy and Microanalysis*, 15(SUPPL 2):292–293, July 2009.

[31] Gault B. De Geuser F. Stephenson L. T. Moody M. P. Muddle B. C. and Ringer S. P. Estimation of the reconstruction parameters for atom probe tomography. *Microscopy and Microanalysis*, 14(4):296–305, August 2008.

[32] Gault B. Moody M. P. De Geuser F. Tsafnat G. La Fontaine A. Stephenson L. T. Haley D. and Ringer S. P. Advances in the calibration of atom probe tomographic reconstruction. *Journal of Applied Physics*, 105(3):034913, 2009.

[33] Menand A. Al Kassab T. Chambreland S. and Sarrau J. M. Aton-probe study of aluminium-lithium alloys. *J. Phys. Colloques*, 49:C6–353–C6–358, 1988.

[34] W. L. Morris. The effect of intermetallics composition and microstructure on fatigue crack initiation in AI 2219-T851. *Metallurgical Transactions A*, 9(9):1345–1348, Sep 1978.

[35] Y. Xue, H. El Kadiri, M.F. Horstemeyer, J.B. Jordon, and H. Weiland. Micromechanisms of multistage fatigue crack growth in a high-strength aluminum alloy. *Acta Materialia*, 55(6):1975–1984, 2007.

[36] M. Mansouri Arani, N.S. Ramesh, X. Wang, N. Parson, M. Li, and W.J. Poole. The localization of plastic deformation in the precipitate free zone of an Al-Mg-Si-Mn alloy. *Acta Mat.*, 231:117872, 2022.

[37] J.F Nye. Some geometrical relations in dislocated crystals. *Acta Metallurgica*, 1(2):153–162, 1953.

[38] W. Pantleon. Resolving the geometrically necessary dislocation content by conventional electron backscattering diffraction. *Scripta Materialia*, 58(11):994–997, 2008.

[39] L.T. Belkacemi, M. Vaidya, A. Hassanpour, F. Jomard, D. Irmer, C. Guerre, L. Martinelli, C. Duhamel, G. Wilde, V.A. Esin, and S.V. Divinski. Intrinsic heterogeneity of grain boundary states in ultrafine-grained Ni: a cross-scale study by SIMS and radiotracer analyses. *Materialia*, page 101397, 2022.

[40] C. Moussa, M. Bernacki, R. Besnard, and N. Bozzolo. About quantitative ebsd analysis of deformation and recovery substructures in pure tantalum. In *IOP Conference Series: Materials Science and Engineering*, volume 89, 2015.

[41] Masayuki Kamaya. Assessment of local deformation using EBSD: Quantification of accuracy of measurement and definition of local gradient. *Ultramicroscopy*, 111(8):1189–1199, 2011.

[42] Waugh A. R. Boyes E. D. and Southon M. J. Investigations of field evaporation with a field-desorption microscope. *Surface Science*, 61(1):109–142, December 1976.

[43] Vurpillot F. Bostel A. and Blavette D. Trajectory overlaps and local magnification in three-dimensional atom probe. *Appl. Phys. Lett.*, 76:3127, July 2000.

[44] Moore A. J. W. The structure of atomically smooth spherical surfaces. *Journal of Physics and Chemistry of Solids*, 23(7):907–912, July 1962.

[45] Vurpillot F. Bostel A. Cadel E. and Blavette D. The spatial resolution of 3d atom probe in the investigation of single-phase materials. *Ultramicroscopy*, 84(3-4):213–224, August 2000.

[46] Ma S. L. Asl K. M. Tansarawiput C. Cantwell P. R. Qi M. H. Harmer M. P. and Luo J. A grain boundary phase transition in si–au. *Scr. Mater.*, 66:203–206, 2012.

[47] Yang S. F. Zhou N. X. Zheng H. Ong S. P. and Luo J. First-order interfacial transformations with a critical point: breaking the symmetry at a symmetric tilt grain boundary. *Phys. Rev. Lett.*, 120:085702, 2018.

[48] Kwiatkowski da Silva A. Ponge D. Peng Z. Inden G. Lu Y. Breen A. Gault B. and Raabe D. Phase nucleation through confined spinodal fluctuations at crystal defects evidenced in fe-mn alloys. *Nat. Commun.*, 9:1137, 2018.

[49] Kwiatkowski da Silva A. Kamachali R. D. Ponge D. Gault B. Neugebauer J. and Raabe D. Thermodynamics of grain boundary segregation, interfacial spinodal and their relevance for nucleation during solid-solid phase transitions. *Acta Mater.*, 168:109–120, 2019.

[50] Zhao H. De Geuser F. Kwiatkowski da Silva A. Szczepaniak A. Gault B. Ponge D. and Raabe D. Segregation assisted grain boundary precipitation in a model al-zn-mg-cu alloy. *Acta Mater.*, 156:318–329, 2018.

[51] Sai Rajeshwari K., S. Sankaran, K.C. Hari Kumar, Harald Rösner, Martin Peterlechner, Vladimir A. Esin, Sergiy Divinski, and Gerhard Wilde. Grain boundary diffusion and grain boundary structures of a Ni-Cr-Fe- alloy: Evidences for grain boundary phase transitions. *Acta Mat.*, 195:501–518, 2020.

[52] Vladimir A. Esin and Boris S. Bokstein. Effect of atomic interaction on grain boundary diffusion in the B regime. *Acta Mat.*, 60(13):5109–5116, 2012.

[53] Vladimir A. Esin and Youssef Souhar. Solvent grain boundary diffusion in binary solid solutions: a new approach to evaluate solute grain boundary segregation. *Philosophical Magazine*, 94(35):4066–4079, 2014.

[54] B. S. Bokshtein, V. A. Esin, and A. O. Rodin. A new model of grain-boundary segregation with the formation of atomic complexes in a grain boundary. *The Physics of Metals and Metallography*, 109(4):316–322, Apr 2010.

[55] James R. Rice. Dislocation nucleation from a crack tip: An analysis based on the Peierls concept. *Journal of the Mechanics and Physics of Solids*, 40(2):239–271, 1992.

[56] D. Hull and D.J. Bacon. Chapter 10 - strength of crystalline solids. In D. Hull and D.J. Bacon, editors, *Introduction to Dislocations (Fifth Edition)*, pages 205–249. Butterworth-Heinemann, Oxford, fifth edition edition, 2011.